Tuning bandgaps in metastructured beams:
numerical and experimental study[*]

Yi YUAN[1], Wei-jian ZHOU[1,2], Jian LI[1], Wei-qiu CHEN[†‡1,3,4], Rong-hao BAO[†‡1,4]

[1]*Key Laboratory of Soft Machines and Smart Devices of Zhejiang Province & Department of Engineering Mechanics,*
Zhejiang University, Hangzhou 310027, China

[2]*Department of Architecture and Civil Engineering, City University of Hong Kong, Hong Kong, China*

[3]*State Key Lab of CAD & CG, Zhejiang University, Hangzhou 310058, China*

[4]*Soft Matter Research Center, Zhejiang University, Hangzhou 310027, China*

[†]E-mail: chenwq@zju.edu.cn; brh@zju.edu.cn

Received July 11, 2019; Revision accepted Sept. 11, 2019; Crosschecked Oct. 10, 2019

Abstract: Tunable metastructures (including phononic crystals and metamaterials) have the unique advantage that one can change the operating frequency and acoustic wave characteristics as needed. In this paper, the bandgap characteristics and their controllability of a metastructured beam with mass-spring oscillators and under an axial force are investigated in depth both by the finite element method and by experiment. The experimental and numerical results indicate that there is one local resonance (LR) bandgap and multiple Bragg scattering (BS) bandgaps. The width and position of each bandgap can be tuned effectively by adjusting the axial force, lattice constant, and spring stiffness, and a super wide pseudo-gap can be obtained under suitable conditions. By integrating different mass-spring oscillators into one metastructured beam, the bandgap width can be broadened and pseudo-gap-like characteristics can be achieved. By changing the number of different oscillators, the propagating distance of elastic waves in the beam can also be controlled. It is further revealed that point defects have a large influence on the BS bandgaps but little effect on the LR bandgap. The present work provides an important reference for the optimal design of adjustable high-performance metastructures.

Key words: Metastructured beam; Prestress; Tunable bandgap; Pseudo-gap; Arrangement

https://doi.org/10.1631/jzus.A1900330　　　　　　　　　　**CLC number:** O32

1 Introduction

When an elastic wave propagates in a phononic crystal (PC, a medium with periodicity in material properties or/and geometry), it will interact with the periodic structure to produce destructive or constructive interference, which can lead to the Bragg scattering (BS) bandgap (Kushwaha et al., 1993; Birkl et al., 1996). If resonant cells are integrated into a medium or structure, they will resonate at certain frequencies and efficiently absorb the wave energy (Liu et al., 2002; Huang and Sun, 2010) to form another type of bandgap, the local resonance (LR) bandgap (Liu et al., 2000). Such a medium is also known as a metamaterial (MM). Generally, there is a limitation for PCs that the center frequency of the first-order BS bandgap is decided by $c/(2L)$, where c is the wave velocity and L is the lattice constant (Zhang et al., 2015). It means that we have to design a large L in

order to obtain the low-frequency BS bandgaps which are critical to applications related to acoustic waves. By contrast, the LR mechanism allows small L to control the low-frequency elastic waves, and hence MMs are not subjected to the above restriction, and it is much easier to get low-frequency bandgaps (Gao et al., 2017; Sheng et al., 2018). The BS bandgaps can exist alone or along with the LR bandgaps, depending on the design of the metastructure (PC or MM). In general, the two types of bandgap are separated from each other by a passband when both mechanisms are present in the metastructure. However, under certain conditions, their neighbouring boundaries may get very close, and accordingly a special super wide pseudo-gap emerges (Xiao et al., 2012), in the center of which is an extremely narrow passband.

One-dimensional structures such as rod, shaft, and beam are widely used in our daily life. Environment-induced vibrations have a great influence on the strength, stiffness, and stability of these structures. Reasonably designed metastructures can reduce the damage caused by the vibrations to a certain extent, and thus have been deeply explored (Yu et al., 2008; Gao and Hou, 2018). However, in the case where the environment and requirements vary from time to time, it is difficult for a metastructure with fixed bandgaps to meet practical needs. In such circumstances, the metastructure with actively tunable bandgaps exhibits great advantages. In recent years, great research progress has been made on actively controlling bandgap characteristics by adopting metastructures with multi-field coupling effects (such as piezoelectric (Rupp et al., 2010; Zhou et al., 2019), dielectric (Yang et al., 2008), electrorheological (Yeh, 2007), and magnetorheological (Bayat and Gordaninejad, 2015)), by applying pre-stress (Bertoldi and Boyce, 2008; Mousavi et al., 2015), or by changing temperature (Huang and Wu, 2005).

Recently, Zhou et al. (2019) carried out a theoretical study on a pre-stressed PC beam with piezoelectric spring oscillators, predicting the existence of super wide pseudo-gap, and giving its appropriate conditions. In this study, we further use numerical and experimental methods to validate the theoretical analysis, and to explore more deeply the effects of lattice constant, spring stiffness, and axial force on the bandgap characteristics. In particular, we demonstrate how to choose the appropriate parameters to obtain an actively tunable, low-frequency, and wide bandgap. The influences on bandgaps of integrating different mass-spring oscillators and of introducing point defects into the metastructured beam are also studied and discussed.

2 Metastructured beam

2.1 Beam model and some theoretical results

The metastructured beam investigated in this study is shown in Fig. 1. It contains three components: the base beam, the springs, and the masses. The springs (with stiffness K) and the masses (with mass M) form the mass-spring oscillators, which are arranged periodically on the base beam. The lattice constant (period length) is L, and the two ends of each spring are connected to the mass and the base beam, respectively. The base beam has a rectangular cross section (with thickness H and width B), and is elastically isotropic (with Young's modulus E, Poisson's ratio v, and density ρ).

In the following analysis, the mass is assumed to be a concentrated one, the base beam is modelled using the Euler-Bernoulli model (Bauchau and Craig, 2009), and the mass of the spring is completely ignored. When a harmonic bending wave $w(x)\mathrm{e}^{-\mathrm{i}\omega t}$ (ω is the angular frequency, $\mathrm{i} = \sqrt{-1}$ is the imaginary unit) propagates in the beam subjected to an axial force N, the deflection amplitude $w(x)$ satisfies the following fourth-order differential equation (Gei et al., 2009):

$$EI\frac{\mathrm{d}^4 w}{\mathrm{d}x^4} - N\frac{\mathrm{d}^2 w}{\mathrm{d}x^2} - \rho A \omega^2 w = 0, \tag{1}$$

where A is the cross-sectional area of the beam, and I is the area moment of inertia with respect to the neutral axis of the base beam. The solution of $w(x)$ is then

$$\begin{aligned} w(x) = &W_1 \cos(\lambda x) + W_2 \sin(\lambda x) \\ &+ W_3 \cosh(\gamma x) + W_4 \sinh(\gamma x), \end{aligned} \tag{2}$$

where

$$\lambda = \sqrt{\frac{-N + \sqrt{N^2 + 4EI\rho A \omega^2}}{2EI}},$$

$$\gamma = \sqrt{\frac{N + \sqrt{N^2 + 4EI\rho A\omega^2}}{2EI}}, \qquad (3)$$

and the coefficients, W_i (i=1, 2, 3, 4), will be determined from the boundary conditions.

For elastic wave propagation in an infinite periodic beam, the physical variables at the two ends of a unit cell should be related through the Bloch theorem (Kittel, 2005), that is

$$V_{j+1}(0) = e^{ikL} V_j(0), \qquad (4)$$

where k is the Bloch number, and the state vector $V(x)$ consists of $w(x)$ (deflection), $w'(x)$ (slope), $-EIw''(x)$ (bending moment), and $-EIw'''(x)$ (shear force). Here the prime denotes a derivative with respect to x.

According to the analysis of Zhou et al. (2019), the edge frequencies of the bandgaps in the beam can be classified into two groups. The first group is associated with the BS bandgaps, given by

$$\omega_{\mathrm{B},n} = \sqrt{\frac{EI(n\pi)^4 + NL^2(n\pi)^2}{\rho AL}}, \quad n = 1, 2, 3, \cdots. \quad (5)$$

The second group, related to the LR bandgap, reads as

$$\frac{\omega^{-2}}{K} = \frac{1}{K} + \frac{\lambda \tanh(\lambda L/2) - \gamma \tan(\lambda L/2)}{2EI\lambda\gamma(\lambda^2 + \gamma^2)}, \qquad (6)$$

$$\frac{\omega^{-2}}{K} = \frac{1}{K} + \frac{\lambda \coth(\lambda L/2) + \gamma \cot(\lambda L/2)}{2EI\lambda\gamma(\lambda^2 + \gamma^2)}. \qquad (7)$$

When the neighbouring boundaries of the BS and LR bandgaps become coincident, a so-called super wide pseudo-gap will form, and the conditions are

$$K = \begin{cases} \dfrac{2n^2\pi^2 EIM\Gamma^2(n^2\pi^2 + \Gamma^2)}{2\rho AL^4(n^2\pi^2 + \Gamma^2) + n^2\pi^2 M\Gamma L^3 \coth(\Gamma/2)}, \\ \qquad\qquad n = 1, 3, 5, \cdots, \\[1em] \dfrac{2n^2\pi^2 EIM\Gamma^2(n^2\pi^2 + \Gamma^2)}{2\rho AL^4(n^2\pi^2 + \Gamma^2) + n^2\pi^2 M\Gamma L^3 \tanh(\Gamma/2)}, \\ \qquad\qquad n = 2, 4, 6, \cdots, \end{cases} \quad (8)$$

where $\Gamma = \sqrt{n^2\pi^2 + NL^2/(EI)}$. As indicated above, K is an increasing function about n and N, so the minimum K that makes the super wide pseudo-gap exist when n=1 and N=0 is

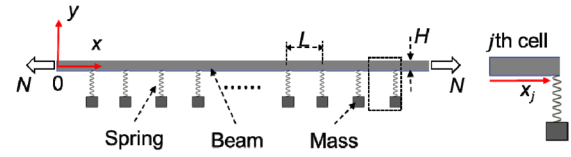$$K_{\min} = \frac{4\pi^4 EIM}{4\rho AL^4 + \pi ML^3 \coth(\pi/2)}. \qquad (9)$$

Fig. 1 Schematic diagram of the metastructured beam
x_j is the local coordinate at the jth cell

2.2 Numerical simulation

In order to verify the above theoretical predictions based on a unit cell using the periodic condition (Zhou et al., 2019), we now develop numerical and experimental methods to make further comparisons and also to carry out extensive parametric studies. The numerical simulation makes use of the finite element method (FEM) based on the commercial software ABAQUS. The mass-spring oscillator is then simulated by adopting concentrated mass and spring-damping modules. The beam can be simulated by wire (1D), shell (2D), or solid (3D) units; they are the most appropriate for a long and thin beam, a thin and wide beam, or a short and thick beam, respectively. Since the base beam is treated theoretically as an Euler-Bernoulli beam in Section 2.1, we also choose the wire unit in the simulation for consistency.

Our simulation focuses on the frequency response spectrum, from which the bandgap characteristics can be easily clarified (Javid et al., 2016). Thus, here we consider a metastructured beam of finite length; its FEM model is shown in Fig. 2. The cross section is rectangular, the same as in the theoretical beam model. The beam is divided into several segments according to the lattice constant, and the joint nodes are marked in the figure. At a position above each node, an attachment point is added, where a concentrated mass can be placed. A spring is finally integrated into the FEM model by connecting it to the

node and the attachment point at its two ends, respectively. It is noted that, in general, we need to adopt a strategy in the numerical simulation that will restrain the boundary reflection in a finite-size beam (e.g. the perfectly matched layer for a finite beam (Chew and Liu, 1996)). However, we have found through comparison that the effect of boundary reflection on the bandgap characteristics is very small and can be neglected. Thus, the FEM results presented in this study are all obtained for a finite-size beam without any special treatment of the boundary reflection.
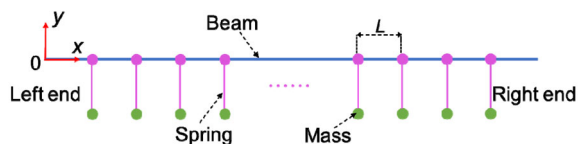

Fig. 2 Schematic diagram of the metastructured beam in ABAQUS

There are several ways to simulate the pre-stress induced by the axial force in ABAQUS, including restarting analysis, applying a specific initial stress field, and using multiple analysis steps. Here we adopt three analysis steps to simulate the dynamic response of a pre-stressed beam: (1) in the initial step, fix the left end of the beam in the x-direction; (2) create a static-general analysis step based on the initial step, turn on the NLGEOM switch, and apply a concentrated tensile force on the right end of the beam; (3) set a steady-state dynamics analysis step, choose the parameters including the frequency range and the step length, and apply the displacement excitation in the y-direction to the right end of the beam. By comparing the wave amplitudes at the two ends of the beam in the frequency range of interest, the bandgap characteristics of the metastructured beam can be finally obtained.

3 Experiment

In the theoretical and numerical analyses, the base beam is modelled based on the Euler-Bernoulli theory, and the effects of the gravity of the beam, the mass of the springs, and the boundary reflections are

all ignored. Correspondingly, in the experiment, it is necessary to select a slender base beam with large stiffness, lightweight springs, and small masses. In addition, the concentrated forces, caused by mass-spring oscillators, applied on the center line of the base beam, will make the base beam deform unevenly along the width direction. The smaller the beam stiffness, the larger the mass (and the spring stiffness and the aspect ratio of the beam as well), and the higher the frequency, the more obvious the uneven effect. Therefore, to reduce the error between the experimental and theoretical/numerical results, we need to make a careful selection of the material and geometric parameters of the metastructured beam. Finally, according to Eq. (9), the spring stiffness must be large enough (at least to approach K_{min}) for the super wide pseudo-gap to exist.

Based on the above considerations, the base beam was made from 6061 aluminum alloy, with Young's modulus E=68.9 GPa, Poisson's ratio v=0.33, and density ρ=2700 kg/m^3. The geometric parameters of the base beam were selected as: length L_b=1.2 m, width B=0.008 m, and thickness H=0.002 m. Five series of springs had the same length of 0.01 m but different diameters, and the stiffnesses were measured by a mechanical testing machine and found to be 4931, 12 892, 19 335, 32 668, and 41 976 N/m, respectively. The mass was made of stainless-steel with the mass being M=0.02 kg.

The schematic diagram and the picture of the experimental setup are shown in Figs. 3 and 4, respectively. The two ends of every spring were bonded to the mass and the center line of the surface of the base beam by glue. The distance between the mass-spring oscillators is L.

In order to reduce the boundary influence and apply the axial forces conveniently, two small holes with a diameter of 3 mm were drilled at a distance of 4 mm from the two ends of the beam, respectively. Soft ropes were used, which pass through the small holes, with the left rope connected to a fixed point to constrain the axial (x-direction) displacement of the beam, and the right rope connected to a weight so as to exert an axial force on and maintain the pre-stress in the base beam. A white noise vibration signal was input at the right end to excite the beam. Lightweight accelerometers were integrated at both ends of the

base beam to collect the dynamic responses, which were transferred to the computer via digital to analog converter (DAC) and then used to calculate the frequency response spectrum.

By hanging different weights, replacing springs of different stiffness, and changing the oscillator spacing, the effects of axial force N, spring stiffness K, and lattice constant L on the bandgap characteristics of the metastructured beam can be studied separately or jointly via the proposed economic and efficient experimental setup.
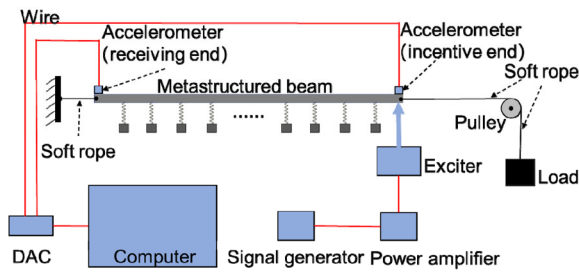

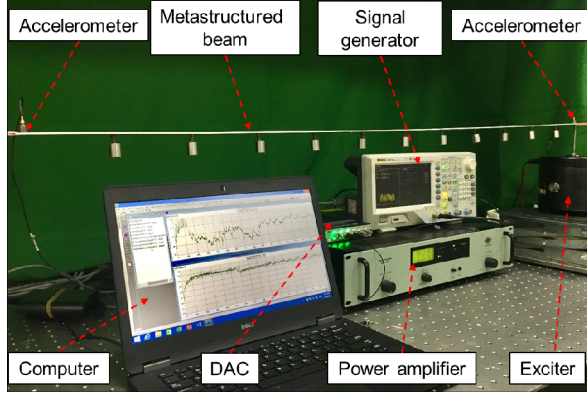**Fig. 3 Schematic diagram of the experimental setup**

Fig. 4 Photo of the experimental setup

4 Results and discussion

In the following, we will adopt dimensionless parameters for convenience of discussion. Therefore, unless specially stated, the reference lattice constant is set to L_0=0.1 m and the reference spring stiffness is K_0=10 000 N/m. Then, we define the dimensionless lattice constant as $\eta_L=L/L_0$, the dimensionless spring stiffness as $\eta_K=K/K_0$, and the dimensionless axial force as $\eta_N=N/(EA)$.

The frequency response spectrum of the metastructured beam calculated by ABAQUS is shown in Fig. 5 for η_K=2, η_L=1, and η_N=0. The quantity S= $20\lg(A_O/A_I)$ (unit: dB) is used to describe the attenuation intensity, where A_O and A_I are the wave amplitudes at the receiving point and the excitation point, respectively. Since the reference intensity of the signal at the excitation point is 0, there is attenuation when S<0 and the signal is enhanced when S>0. As can be seen from Fig. 5, in the range of 0–1200 Hz, there are two bandgaps in the metastructured beam: the one with lower frequency and stronger attenuation is the LR bandgap, while the other one with higher frequency and weaker attenuation is the BS bandgap. The bottom gray bar is determined by S. The darker the color, the stronger the attenuation, while the white stripes represent the formants. Therefore, the gray bar can also describe the bandgap characteristics of the metastructured beam. Fig. 6 shows the wave propagation when the frequency is in the bandgap or in the passband, from which the amplitude attenuation or maintenance can be seen clearly.
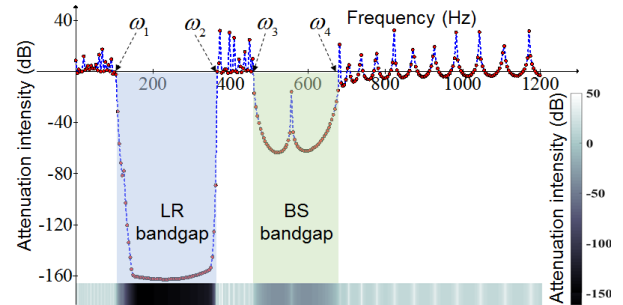

Fig. 5   Frequency response spectrum calculated by ABAQUS (η_K=2, η_L=1, and η_N=0). ω_1–ω_4 are edge frequencies of bandgaps
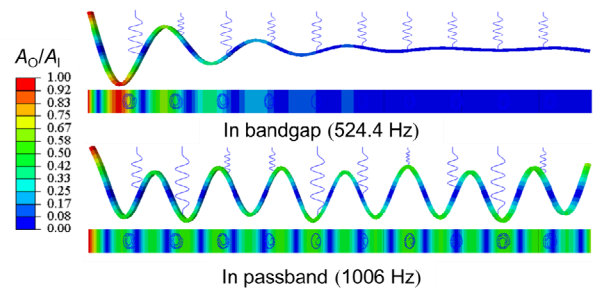

Fig. 6 Wave propagation when the frequency is in the bandgap or passband (η_K=2, η_L=1, and η_N=0)

4.1 Effects of lattice constant, spring stiffness, and axial force on bandgaps

We have the following relationship between the frequency and the lattice constant L:

$$f_B = \frac{c}{2L}, \qquad (10)$$

where f_B is the center frequency of the first-order BS bandgap, and c is the wave velocity in the base beam (Zhang et al., 2015). Thus, the larger the lattice constant L, the lower the corresponding frequency.

Fig. 7 shows the effect of the dimensionless lattice constant η_L on the bandgap while the dimensionless spring stiffness and axial force are fixed as $\eta_K=5$ and $\eta_N=0$. The gray bars in the figure are determined by the attenuation intensity from the FEM simulations. The solid lines, which are fitted by the numerical results, can reflect the continuous change of the bandgap edge frequencies. The dots represent the edge frequencies predicted by the theoretical model, and the dashed line represents the natural frequency of the mass-spring resonator. It can be seen that the finite element results agree very well with the theoretical results. When η_L increases from 0.5 to 3.0, the number of bandgaps increases from 1 to 6, while the edge frequencies decrease and the widths of the two lowest-order bandgaps become narrower.

These positions, where the boundaries of the BS bandgap and the LR bandgap coincide, are called the turn points (TPs), and the first three TPs are shown in Fig. 7. The darkest bandgap in every bar represents the LR bandgap, whose position is exchanged with that of the BS bandgap at TPs gradually from the 1st bandgap to the 4th bandgap. When TP exists, the neighbouring boundaries of two bandgaps coincide to form a so-called super wide pseudo-gap (Zhou et al., 2019), and this formation condition is expressed by Eq. (8). Observing the position of the dashed line, we can find that the natural frequency of the mass-spring resonator can be located in the LR bandgap, or in the BS bandgap, or even in the passband.

Fig. 8 compares the experimental results with the FEM simulations. It is seen that the bandgap widths and positions predicted by the two methods are generally consistent with each other.
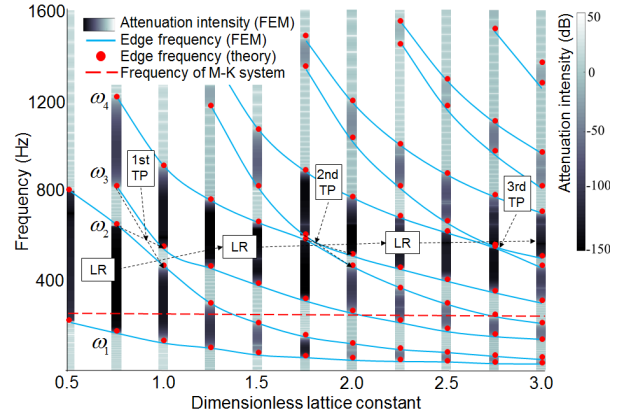

Fig. 7 Effect of η_L on bandgaps (M-K system means mass-spring system; LR means local resonant bandgap; TP means turn point where the boundaries of the BS bandgap and the LR bandgap coincide. $\eta_K=5$, $\eta_N=0$)
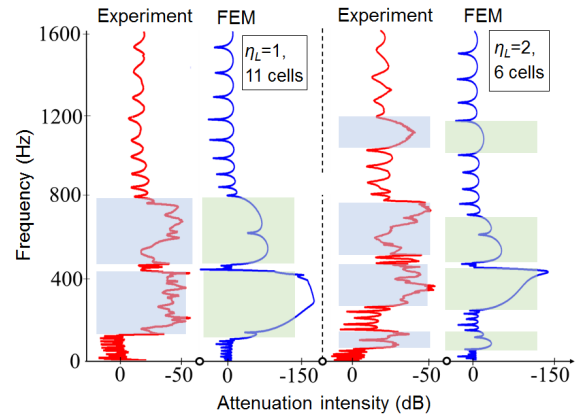

Fig. 8 Effect of η_L on bandgaps ($\eta_K=3.3$, $\eta_N=2.72\times10^{-5}$)

Fig. 9 shows the effect of the dimensionless spring stiffness η_K on the bandgaps in the metastructured beam. As η_K increases, the edge frequency ω_4 increases all the time, while ω_1 increases slowly and then stabilizes to a fixed value. After the 1st TP, ω_2 stabilizes at the first-order Bragg frequency, and ω_4 increases with the trend previously possessed by ω_2. It can be judged by the position of the dark region that the LR bandgap and the BS bandgap are also exchanged at the 1st TP. In general, with the dimensionless spring stiffness η_K increasing, the bandgap edge frequency and width increase. The width of the passband between the first two bandgaps decreases first and then increases, and at the 1st TP, the passband almost disappears, forming a super wide pseudo-gap.

When an axial force is applied to the beam, the effective stiffness of the beam (before buckling) will increase. As can be seen from Fig. 10, with η_N increasing, the edge frequencies of the BS bandgap increase, while the edge frequency ω_1 of the LR bandgap increases slowly and finally approaches the natural frequency of the mass-spring resonator, and ω_2 remains almost unchanged after the 1st TP. The bandgap width becomes wider first and then narrower, and a pseudo-gap appears at the 1st TP (near η_N=1.5).
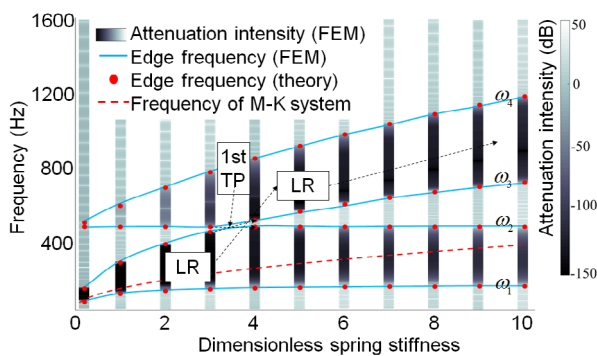

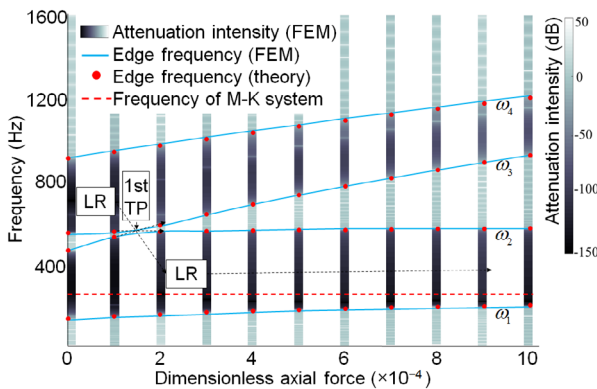**Fig. 9 Effect of η_K on bandgaps (η_L=1, η_N=0)**

Fig. 10 Effect of η_N on bandgaps (η_L=1, η_K=5)

4.2 Super wide pseudo-gap

According to the previous discussion, it can be concluded that under certain conditions, such as at TPs in Fig. 7, the boundaries of the LR and BS bandgaps will coincide, and the passband between the two bandgaps becomes extremely narrow, forming a so-called super wide pseudo-gap. In this study, we just pay attention to the first two lowest pseudo-gaps

(n=1 and n=2 in Eq. (8)). Satisfying the formation condition in Eq. (8), the three dimensionless parameters (η_L, η_K, and η_N) are not all independent. In the following, we fix η_L=1, while choosing η_N as the main parameter to study for its effect on the pseudo-gap.

Figs. 11 and 12 show the variations of the super wide pseudo-gaps with the dimensionless axial force η_N when n=1 and n=2 in Eq. (8), respectively. The dotted line represents the extremely narrow passband (near η_N=1.5). As η_N increases, the width of each pseudo-gap increases. When n=1, the ratio of bandgap width to total width (($\omega_4-\omega_1$)/ω_4) exceeds 85.3% from 0 Hz to ω_4; when n=2, the ratio (($\omega_6-\omega_3+\omega_2-\omega_1$)/$\omega_6$) exceeds 77.8% from 0 Hz to ω_6. If an elastic wave filter is designed based on this characteristic, elastic waves whose frequencies are in the narrow passband can be selected out over a super wide frequency range, and the larger the η_N, the better the filtering effect.
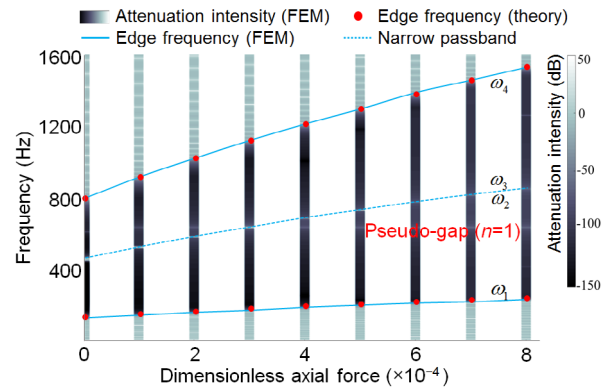

Fig. 11 Effect of η_N on the super wide pseudo-gap when n=1 (η_L=1)
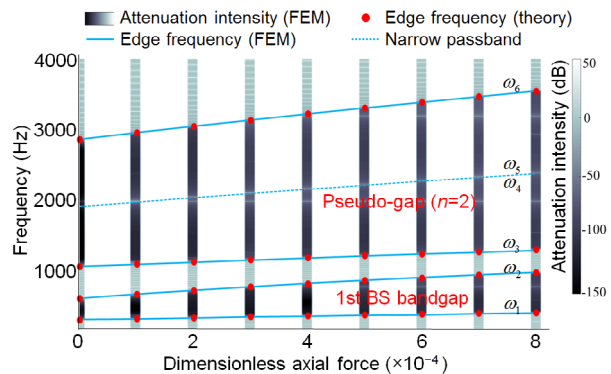

Fig. 12 Effect of η_N on the super wide pseudo-gap when n=2 (η_L=1)

Fig. 13 shows the comparison between the experimental and numerical results when $\eta_N=2.8\times10^{-5}$, $\eta_K=3.3$, and $\eta_N=5.5\times10^{-5}$, $\eta_K=4.2$. It should be noted that the corresponding η_K for $\eta_N=2.8\times10^{-5}$ and $\eta_N=5.5\times10^{-5}$ are 3.655 and 3.966 respectively under the formation conditions of a super wide pseudo-gap, which are close to the parameters used in the experiment. It can be seen that the passband between the two lowest bandgaps is relatively narrow, giving rise to the super wide pseudo-gap.
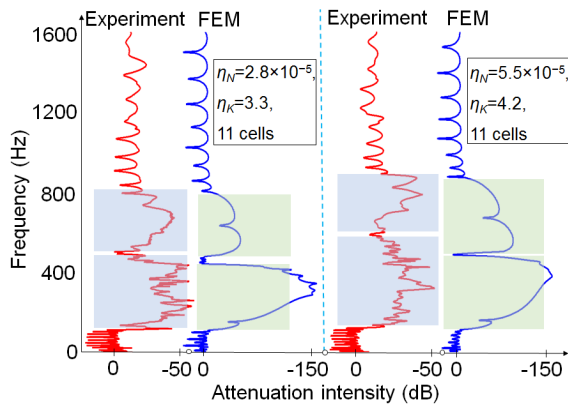

Fig. 13 Comparison between the experimental and numerical results ($\eta_L=1$)

4.3   One-dimensional tandem metastructured beam

When an elastic wave propagates in the metastructured beam, the wave amplitude will be attenuated or enhanced. If different metastructured models are connected in series or in tandem, the wave propagation behavior will be a comprehensive result. If the attenuation is greater than the enhancement, the synthesized structure can achieve the effect of widening bandgaps (Zhu et al., 2014; Barnhart et al., 2019). This feature has been used to construct 1D layered PCs with an ultra-wide bandgap (Kushwaha, 2008; Chen et al., 2017) as well as metamaterials with broadband wave mitigation at subwavelength scale (Chen et al., 2016; Xu et al., 2019).

From Fig. 9, it is seen that the edge frequency ω_3 before TP is the same as ω_2 after TP. If two pairs of mass-spring oscillators (A and B), selected from both sides of TP, are arranged in the way as shown in Fig. 14, the new metastructured beam is expected to

have much wider bandgaps and the analogous pseudo-gaps. In the following discussion, the synthesized beam is named AB, while the one with only springs A (or B) is named AA (or BB).
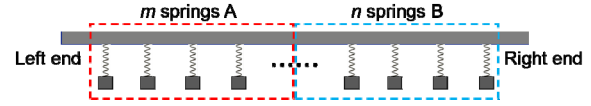

Fig. 14 Two metastructured beams with different mass-spring resonators connected in series to form a new synthesized metastructured beam

Taking $\eta_{KA}=3$, $\eta_{KB}=4$, $m=10$, and $n=9$, input the vibration signal at the left end of the beam, and receive the signal at the right end. The FEM results are shown in Fig. 15. It is seen that the edge frequency ω_1 of AB is very close to AA, while ω_4 of AB is very close to BB. The original passband between the two bandgaps of AA (or BB) becomes a bandgap in AB, with only a very narrow frequency range acting like a passband. In this case, AB exhibits similar characteristics to a super wide pseudo-gap. In fact, the result of a tandem structure can be approximated as a weighted average of the results of individual structures, and the weighting factors are related to the number of the respective resonators (Deymier, 2013), which are $m/(m+n)$ and $n/(m+n)$. Fig. 16 shows the comparison between the directly calculated result of AB by ABAQUS and the approximate result using the above weighted formula, which is $S_{AB}=(mS_{AA}+nS_{BB})/(m+n)$. It is seen that the bandgap characteristics from the two methods match quite well with each other. Therefore, the bandgap characteristics of the tandem structure can be approximately predicted from Fig. 9. Obviously, we can integrate other springs, masses, or lattice constant L, to form a synthesized metastructured beam, so as to obtain much wider bandgaps and a super wide pseudo-gap according to Figs. 7, 9, and 10.

In addition, it is very effective to control the propagation distance of an elastic wave at certain frequencies in the synthesized beam by adjusting m and n. Fig. 17 shows the wave propagation in the beam with m ($\eta_K=1$) and n ($\eta_K=3$) mass-spring oscillators at 385 Hz while keeping $m+n=19$. It is seen that when m equals 6, 10, and 13, the wave propagation distances are roughly $7L$, $11L$, and $14L$, respectively,

indicating that the wave propagation distance in the beam can be effectively controlled.
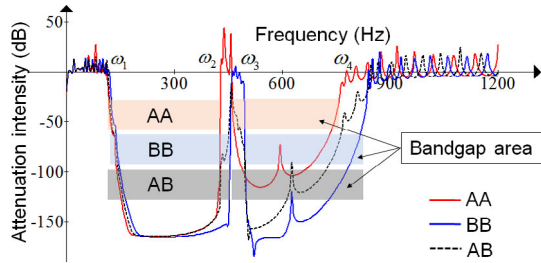

Fig. 15 Comparison of frequency response spectrum between AB and AA or BB (η_L=1, η_N=0)
AB represents the tandem structure of 10 springs A and 9 springs B, while AA (or BB) represents the beam with 19 springs A (or B)
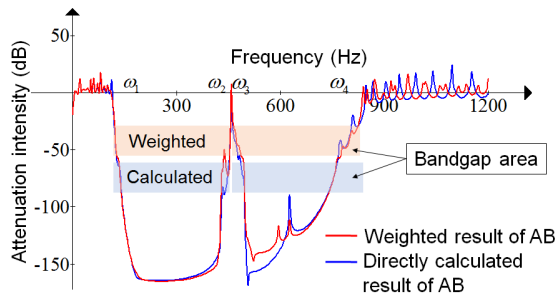

Fig. 16 Comparison of frequency response spectrum between the weighted result and the directly calculated result of AB
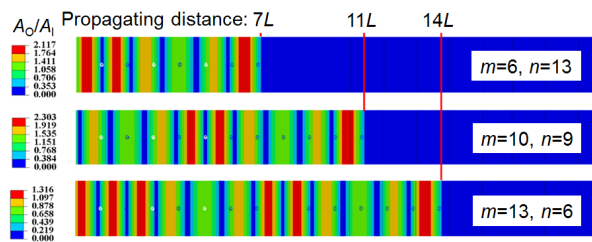

Fig. 17 Control of wave propagation distance by changing the numbers of two different mass-spring oscillators, and *m* (or *n*) is the number of springs A (or B)

4.4 Effect of defect

Defect, which is an important topic in the research of PCs, can cause wave localization (Figotin and Klein, 1996), energy accumulation, wave guiding (Miyashita, 2005; Yao et al., 2010), and other special phenomena. Wave propagation in some periodic structures can be very sensitive to defects, while it may be insensitive to defects in other situations. For the 1D metastructured beam considered in this study, we mainly discuss the influence of point defects (lost mass-spring oscillators) on the bandgaps. Fig. 18 shows the effect of defect when η_L=1, η_N=0, and η_K=1.3. There are 10 mass-spring units, and the 3rd and 7th oscillators represent the third and seventh mass-spring oscillators from the excitation end. The experimental and finite element results show that the omission of a few mass-spring oscillators has little effect on the global bandgap characteristics, especially on the LR bandgap. However, the upper edge frequency ω_4 of the BS bandgap is sensitive to the defects, and the more the defects, the lower the ω_4, and the weaker the attenuation. If the point defects increase, the BS bandgap will gradually disappear.
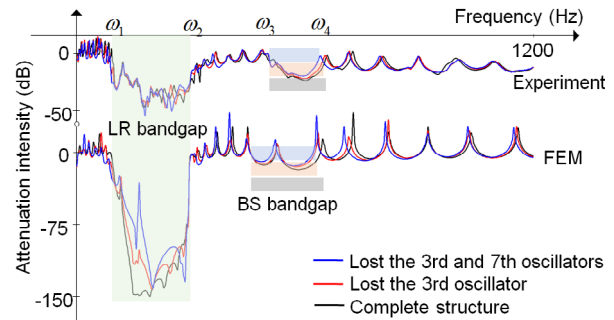

Fig. 18 Effect of point defects on bandgaps (η_L=1, η_N=0, and η_K=1.3)

5 Conclusions

Combined with the theoretical analysis of Zhou et al. (2019), the effects of lattice constant, axial force, and spring stiffness on the bandgap characteristics of a 1D pre-stressed metastructured beam with mass-spring oscillators were investigated by experimental and numerical methods. It was proved that the width and position of the bandgaps can be adjusted by co-operatively changing the axial force and the spring stiffness. In particular, under certain conditions, a super wide pseudo-gap will form. The influences of serial combination and local defect on the bandgaps were also discussed. The main conclusions of this study are summarized as follows:

1. Coordinately changing the lattice constant, axial force, and spring stiffness can effectively adjust the width and position of the bandgaps. Under certain conditions, a super wide pseudo-gap can be obtained, and the larger the axial force, the better the filtering effect based on the narrow passband in the pseudo-gap.

2. The synthesized metastructured beam with two kinds of mass-spring oscillators selected from both sides of TP has much wider bandgaps and an analogous super wide pseudo-gap. At the same time, changing the number of different mass-spring oscillators can effectively control the wave propagation distance in the beam.

3. The point defects have less influence on the LR bandgap but greater influence on the BS bandgaps. If the number of point defects increases, the BS bandgap will be narrowed and even disappear.

It should be pointed out that, although the experimental results are in good agreement with the numerical results, there are still some deviations between them. The errors mainly arise from the experiment, such as an imprecise measurement of the spring stiffness, the position offset of the springs on the beam, and the influence of gravity on the structure. In addition, the inadequacies of the experiment include the fact that the spring stiffness and the axial force cannot be continuously changed, resulting in an inability to obtain the accurate characteristics of the super wide pseudo-gap. In addition, the spring stiffness is relatively small, resulting in a failure to verify the bandgap characteristics with high spring stiffness and high-order pseudo-gaps. In further studies, we will improve the experimental setup and try to lay a more solid foundation for engineering applications.

Contributors

Yi YUAN and Wei-jian ZHOU designed the research. Yi YUAN, Jian LI, and Rong-hao BAO conducted the research and investigation process. Yi YUAN wrote the first draft of the manuscript. Wei-qiu CHEN helped to organize the manuscript. Wei-qiu CHEN and Yi YUAN revised and edited the final version.

Conflict of interest

Yi YUAN, Wei-jian ZHOU, Jian LI, Wei-qiu CHEN, and Rong-hao BAO declare that they have no conflict of interest.

References

Barnhart MV, Xu XC, Chen YY, et al., 2019. Experimental demonstration of a dissipative multi-resonator metamaterial for broadband elastic wave attenuation. *Journal of Sound and Vibration*, 438:1-12.
https://doi.org/10.1016/j.jsv.2018.08.035

Bauchau OA, Craig JI, 2009. Structural Analysis. Springer, Dordrecht, USA, p.173-221.

Bayat A, Gordaninejad F, 2015. Band-gap of a soft magnetorheological phononic crystal. *Journal of Vibration and Acoustics*, 137(1):011011.
https://doi.org/10.1115/1.4028556

Bertoldi K, Boyce MC, 2008. Mechanically triggered transformations of phononic band gaps in periodic elastomeric structures. *Physical Review B*, 77(5):052105.
https://doi.org/10.1103/physrevb.77.052105

Birkl G, Gatzke MA, Deutsch IH, et al., 1996. Bragg scattering from an optical lattice. *Optics and Photonics News*, 7(12):25.
https://doi.org/10.1364/OPN.7.12.000025

Chen H, Li XP, Chen YY, et al., 2017. Wave propagation and absorption of sandwich beams containing interior dissipative multi-resonators. *Ultrasonics*, 76:99-108.
https://doi.org/10.1016/j.ultras.2016.12.014

Chen YY, Barnhart MV, Chen JK, et al., 2016. Dissipative elastic metamaterials for broadband wave mitigation at subwavelength scale. *Composite Structures*, 136:358-371.
https://doi.org/10.1016/j.compstruct.2015.09.048

Chew WC, Liu QH, 1996. Perfectly matched layers for elastodynamics: a new absorbing boundary condition. *Journal of Computational Acoustics*, 4(4):341-359.
https://doi.org/10.1142/S0218396X96000118

Deymier PA, 2013. Acoustic Metamaterials and Phononic Crystals. Springer, Berlin, Germany, p.176-177.

Figotin A, Klein A, 1996. Localization of classical waves I: acoustic waves. *Communications in Mathematical Physics*, 180(2):439-482.
https://doi.org/10.1007/bf02099721

Gao NS, Hou H, 2018. Sound absorption characteristic of micro-helix metamaterial by 3D printing. *Theoretical and Applied Mechanics Letters*, 8(2):63-67.
https://doi.org/10.1016/j.taml.2018.02.001

Gao NS, Hou H, Mu YH, 2017. Low frequency acoustic properties of bilayer membrane acoustic metamaterial with magnetic oscillator. *Theoretical and Applied Mechanics Letters*, 7(4):252-257.
https://doi.org/10.1016/j.taml.2017.06.001

Gei M, Movchan AB, Bigoni D, 2009. Band-gap shift and defect-induced annihilation in prestressed elastic structures. *Journal of Applied Physics*, 105(6):063507.
https://doi.org/10.1063/1.3093694

Huang GL, Sun CT, 2010. Band gaps in a multiresonator

acoustic metamaterial. *Journal of Vibration and Acoustics*, 132(3):031003.
https://doi.org/10.1115/1.4000784

Huang ZG, Wu TT, 2005. Temperature effect on the bandgaps of surface and bulk acoustic waves in two-dimensional phononic crystals. *IEEE Transactions on Ultrasonics, Ferroelectrics, and Frequency Control*, 52(3):365-370.
https://doi.org/10.1109/TUFFC.2005.1417258

Javid F, Wang P, Shanian A, et al., 2016. Architected materials with ultra-low porosity for vibration control. *Advanced Materials*, 28(28):5943-5948.
https://doi.org/10.1002/adma.201600052

Kittel C, 2005. Introduction to Solid State Physics, 8th Edition. John Wiley & Sons, New York, USA, p.167-168.

Kushwaha M, 2008. Ultra-wide-band filter for noise control. *The Journal of the Acoustical Society of America*, 124(4): 2488.
https://doi.org/10.1121/1.4782772

Kushwaha MS, Halevi P, Dobrzynski L, et al., 1993. Acoustic band structure of periodic elastic composites. *Physical Review Letters*, 71(13):2022-2025.
https://doi.org/10.1103/PhysRevLett.71.2022

Liu ZY, Zhang XX, Mao YW, et al., 2000. Locally resonant sonic materials. *Science*, 289(5485):1734-1736.
https://doi.org/10.1126/science.289.5485.1734

Liu ZY, Chan CT, Sheng P, 2002. Three-component elastic wave band-gap material. *Physical Review B*, 65(16): 165116.
https://doi.org/10.1103/PhysRevB.65.165116

Miyashita T, 2005. Sonic crystals and sonic wave-guides. *Measurement Science and Technology*, 16(5):R47-R63.
https://doi.org/10.1088/0957-0233/16/5/R01

Mousavi SH, Khanikaev AB, Wang Z, 2015. Topologically protected elastic waves in phononic metamaterials. *Nature Communications*, 6(1):8682.
https://doi.org/10.1038/ncomms9682

Rupp CJ, Dunn ML, Maute K, 2010. Switchable phononic wave filtering, guiding, harvesting, and actuating in polarization-patterned piezoelectric solids. *Applied Physics Letters*, 96(11):111902.
https://doi.org/10.1063/1.3341197

Sheng X, Zhao CY, Yi Q, et al., 2018. Engineered metabarrier as shield from longitudinal waves: band gap properties and optimization mechanisms. *Journal of Zhejiang University-SCIENCE A (Applied Physics & Engineering)*, 19(9):663-675.
https://doi.org/10.1631/jzus.A1700192

Xiao Y, Wen JH, Wen XS, 2012. Flexural wave band gaps in locally resonant thin plates with periodically attached spring-mass resonators. *Journal of Physics D: Applied Physics*, 45(19):195401.
https://doi.org/10.1088/0022-3727/45/19/195401

Xu XC, Barnhart MV, Li XP, et al., 2019. Tailoring vibration suppression bands with hierarchical metamaterials containing local resonators. *Journal of Sound and Vibration*, 442:237-248.
https://doi.org/10.1016/j.jsv.2018.10.065

Yang WP, Wu LY, Chen LW, 2008. Refractive and focusing behaviours of tunable sonic crystals with dielectric elastomer cylindrical actuators. *Journal of Physics D: Applied Physics*, 41(13):135408.
https://doi.org/10.1088/0022-3727/41/13/135408

Yao ZJ, Yu GL, Wang YS, et al., 2010. Propagation of flexural waves in phononic crystal thin plates with linear defects. *Journal of Zhejiang University-SCIENCE A (Applied Physics & Engineering)*, 11(10):827-834.
https://doi.org/10.1631/jzus.a1000123

Yeh JY, 2007. Control analysis of the tunable phononic crystal with electrorheological material. *Physics B: Condensed Matter*, 400(1-2):137-144.
https://doi.org/10.1016/j.physb.2007.06.030

Yu DL, Wen JH, Zhao HG, et al., 2008. Vibration reduction by using the idea of phononic crystals in a pipe-conveying fluid. *Journal of Sound and Vibration*, 318(1-2):193-205.
https://doi.org/10.1016/j.jsv.2008.04.009

Zhang Y, Han L, Jiang LH, et al., 2015. Phononic Crystal Calculation Method and Band Gap Properties. Science Press, Beijing, China, p.9 (in Chinese).

Zhou WJ, Wu B, Su YP, et al., 2019. Tunable flexural wave band gaps in a prestressed elastic beam with periodic smart resonators. *Mechanics of Advanced Materials and Structures*, 1-8.
https://doi.org/10.1080/15376494.2018.1553261

Zhu R, Liu XN, Hu GK, et al., 2014. A chiral elastic metamaterial beam for broadband vibration suppression. *Journal of Sound and Vibration*, 333(10):2759-2773.
https://doi.org/10.1016/j.jsv.2014.01.009

中文概要

题　目：带隙可调的超结构梁：数值和实验研究

目　的：1. 研究晶格常数、预应力和弹簧刚度对超结构梁带隙的影响，优化结构并形成伪禁带或低频且宽的禁带；2. 通过实验验证伪禁带的存在性、排列对带隙的影响以及缺陷对带隙的影响等。

创新点：1. 通过预应力调节超结构梁的带隙特征，并可以形成伪禁带；2. 通过排列不同弹簧振子构成宽频禁带和宽频伪禁带。

方　法：1. 通过有限元软件模拟预应力、弹簧刚度和晶格常数等参数对该超结构梁带隙的影响情况；2. 设计合适的参数并进行结构优化，使得该结构的带隙宽，频率低，且易于实验实现；3. 在实验中通

过替换弹簧、改变弹簧间距和施加轴向拉力分别研究弹簧刚度、晶格常数和预应力的影响，并通过移除部分弹簧和同时布置不同弹簧的方式研究缺陷和排列对带隙的影响。

结　论： 1. 该结构存在一条局域共振禁带和多条布拉格散射禁带；通过调节预应力、弹簧刚度和晶格常数等可以有效地控制带隙特征。2. 在特定条件下可以形成宽频伪禁带；通过排列不同弹簧振子可以达到拓宽禁带、形成宽频伪禁带的效果。3. 缺陷对布拉格散射禁带的影响较大，对局域共振禁带的影响较小。

关键词： 超结构梁；预拉伸；可调带隙；伪禁带；排列